Science Advances

Supplementary Materials for

Photo-induced cascaded harmonic and comb generation in silicon nitride microresonators

Jianqi Hu *et al.*

Corresponding author: Camille-Sophie Brès, camille.bres@epfl.ch

This PDF file includes:

Supplementary Text
Figs. S1 to S5

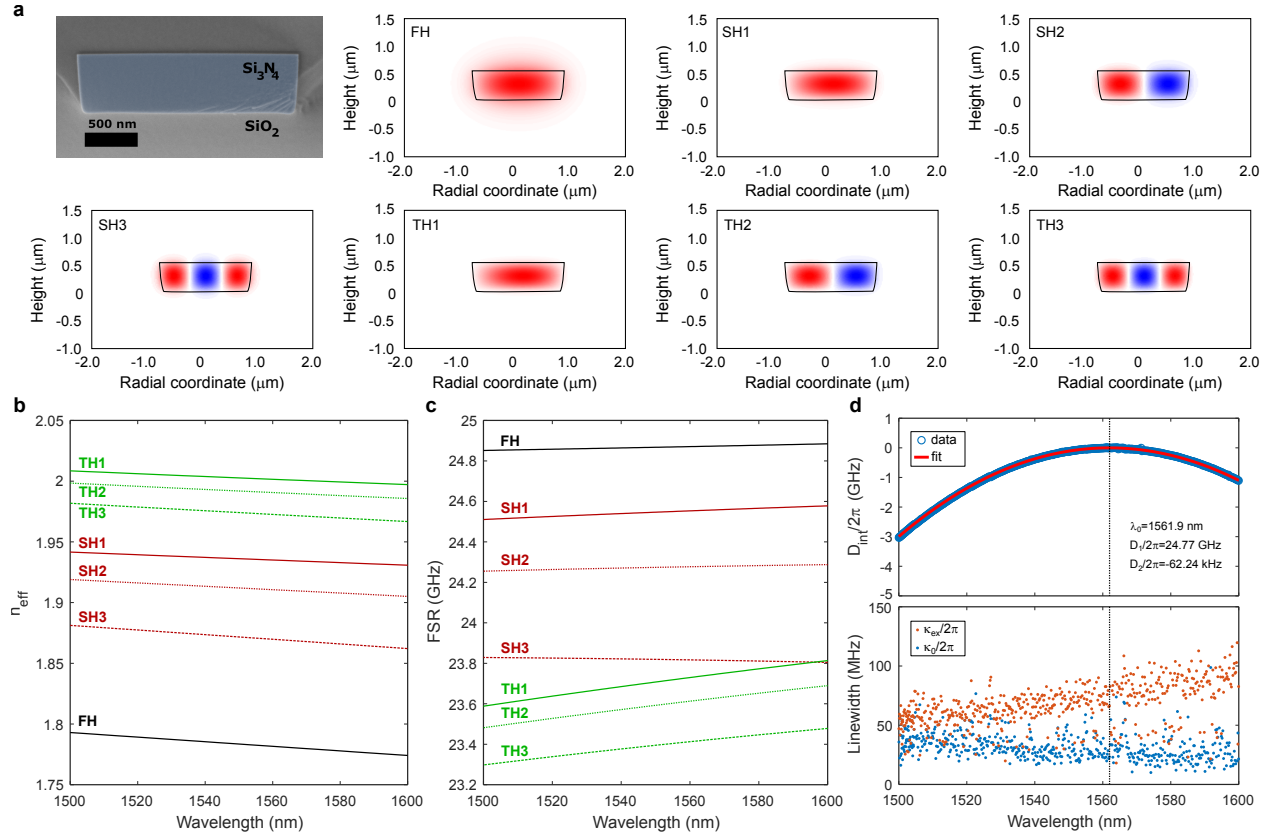# Supplementary Note 1. Characterization and simulation of the Si_3N_4 microresonator

Figure S1: Characterization and simulation of the Si_3N_4 microresonator. a A scanning electron microscope (SEM) image of the waveguide cross-section of the microresonator, along with simulated TE-polarized mode field distributions of fundamental mode at FH wavelength ($\sim 1550\,\text{nm}$), first three SH modes (SH1-SH3) and first three effective TH (TH1-TH3) modes. **b** Simulated effective refractive indices of FH, SH1-SH3, and TH1-TH3 modes with respect to the pump wavelength. **c** Simulated FSRs of the same modes in **b** with respect to the pump wavelength. **d** Top: measured integrated dispersion of the microresonator $D_{\text{int}}/2\pi$ and fit. Bottom: measured intrinsic linewidths ($\kappa_0/2\pi$) and coupling strengths ($\kappa_{\text{ex}}/2\pi$) of resonances at FH.

We utilize a scanning electron microscope (SEM) to accurately retrieve the waveguide cross-section of the used Si_3N_4 microresonator. The measured SEM image is shown in Figure S1a, where the waveguide core is highlighted, and its actual cross-section (width×height) is estimated to be $2150\,\text{nm} \times 572\,\text{nm}$. Based on the retrieved waveguide dimension, we use COMSOL Mul-

tiphysics to simulate the effective refractive indices of the optical modes involved in this study. Figure S1a also displays the simulated TE-polarized mode field distributions for the fundamental mode at FH wavelength ($\sim$ 1550 nm), first three SH modes (SH1 to SH3) as well as first three effective TH modes (TH1 to TH3). For the same set of modes, Figures S1b and c depict the simulated effective refractive indices and FSR values, respectively, as a function of the pump wavelength in the range from 1500 nm to 1600 nm. The effective refractive indices and field distributions of various modes are essential for $\chi^{(2)}$ grating simulation, while their FSRs are important for the comb study. We also employ the frequency-comb-assisted diode laser spectroscopy to measure the resonance linewidths and the dispersion profile of the microresonator (68). The top graph in Figure S1d shows the measured integrated dispersion with respect to the resonance frequency at $\omega_0/2\pi = 191.94$ THz, defined as $D_{\text{int}}(\mu) = \omega_\mu - \omega_0 - D_1\mu = D_2\mu^2/2 + ...$, where $\omega_\mu/2\pi$ is the frequency of the μ-th order resonance, $D_1/2\pi = 24.77$ GHz is the microresonator's FSR, and $D_2/2\pi = -62.24$ kHz is the group-velocity dispersion parameter. This indicates the microresonator is normal dispersion in the wavelength range from 1500 nm to 1600 nm, and no significant avoided mode crossing is observed in the integrated dispersion curve. The bottom graph in Figure S1d shows the measured intrinsic linewidths $\kappa_0/2\pi$ and coupling strengths $\kappa_{\text{ex}}/2\pi$ of the microresonator, which are around 30 MHz and 60 MHz at the pumped wavelength, respectively.

Supplementary Note 2. Modulational instability gain analysis

The FH and SH fields inside the microresonator can be described by mean-field coupled Lugiato–Lefever equations (LLEs) (49, 58):

$$\frac{\partial A}{\partial t} = -(\frac{\kappa_{\text{a}}}{2} + i\delta_{\text{a}})A + i\frac{D_{2,\text{a}}}{2}\frac{\partial^2 A}{\partial \phi^2} + i(\gamma_{\text{aa}}|A|^2 + \gamma_{\text{ba}}|B|^2)A + igBA^* + \sqrt{\kappa_{\text{ex,a}}}s_{\text{in}} \quad (1)$$

$$\frac{\partial B}{\partial t} = -(\frac{\kappa_{\text{b}}}{2} + i\delta_{\text{b}})B - \Delta D_1\frac{\partial B}{\partial \phi} + i\frac{D_{2,\text{b}}}{2}\frac{\partial^2 B}{\partial \phi^2} + i(\gamma_{\text{ab}}|A|^2 + \gamma_{\text{bb}}|B|^2)B + ig^*A^2 \quad (2)$$

where A and B are respectively the temporal envelopes of intracavity FH and SH in the moving frame of FH, normalized such that their modulus squares correspond to the intacavity photon numbers. t is the slow time axis, ϕ is the azimuthal angle along the circumference. $\sqrt{\kappa_{\text{ex,a}}}s_{\text{in}}$

represents the external driving term at pump, with $\kappa_{\text{ex,a}}$ the FH external coupling rate and $|s_{\text{in}}|^2$ the driving power. $\kappa_{\text{a(b)}}$ and $D_{2,\text{a(b)}}$ denote the total loss rate and dispersion at FH (SH), respectively. $\delta_{\text{a}} = \omega_{\text{a}} - \omega$ and $\delta_{\text{b}} = \omega_{\text{b}} - 2\omega$ are the detunings at FH and SH, with $\omega_{\text{a,b}}$ the cold-cavity resonance frequency closest to $\omega(2\omega)$ and ω the pump driving frequency. $\Delta D_1 = D_{1,\text{b}} - D_{1,\text{a}}$ describes the walk-off between FH and SH. $\gamma_{\text{aa(bb)}}$ and $\gamma_{\text{ab(ba)}}$ correspond to the Kerr frequency shifts per photon due to self-phase modulation and cross-phase modulation at FH (SH). g describes the FH-SH coupling strength through the photo-induced $\chi^{(2)}$ QPM grating.

Reasonable assumptions are made before carrying out the modulational instability (MI) analysis. The dispersion term at SH is dropped out due to the large first-order walk-off term. We also consider the case in the limit of $|A|^2 \gg |B|^2$ so that the Kerr frequency shifts are dominated by the FH power for both FH and SH. Under these assumptions, the stationary solutions of coupled LLEs write:

$$\left(\frac{\kappa_{\text{a}}}{2} + i\delta_{\text{a}} - i\gamma_{\text{aa}}|A_0|^2 + \frac{|gA_0|^2}{\frac{\kappa_{\text{b}}}{2} + i\delta_{\text{b}} - i\gamma_{\text{ab}}|A_0|^2}\right)A_0 = \sqrt{\kappa_{\text{ex,a}}}s_{\text{in}} \tag{3}$$

$$B_0 = \frac{ig^*A_0^2}{\frac{\kappa_{\text{b}}}{2} + i\delta_{\text{b}} - i\gamma_{\text{ab}}|A_0|^2} \tag{4}$$

where A_0 and B_0 are flat solutions of FH and SH, respectively. For MI analysis, we consider the ansatz form of the FH field as $A = A_0 + a_1e^{i\mu\phi} + a_2e^{-i\mu\phi}$, where a_1 and a_2 serve as weak perturbation to A_0 at mode indices $\pm\mu$, respectively. By assuming the SH field evolves slowly ($\frac{\partial B}{\partial t} \approx 0$) (58), the perturbation at SH field can be calculated based on Eq. (2) to the first-order approximation:

$$\begin{aligned} B \approx B_0 + b_1e^{i\mu\phi} + b_2e^{-i\mu\phi} = &B_0 + [\gamma_{\text{ab}}B_0(A_0^*a_1 + A_0a_2^*) + 2g^*A_0a_1]J(\mu)e^{i\mu\phi} \\ &+ [\gamma_{\text{ab}}B_0(A_0^*a_2 + A_0a_1^*) + 2g^*A_0a_2]J(-\mu)e^{-i\mu\phi} \end{aligned} \tag{5}$$

where we introduce a walk-off function $J(\mu) = \frac{i}{\frac{\kappa_{\text{b}}}{2} + i\delta_{\text{b}} - i\gamma_{\text{ab}}|A_0|^2 + i\Delta D_1\mu}$ to simplify the expression of b_1 and b_2. Notably, the walk-off function $J(\mu)$ is basically a lineshape function with the linewidth given by the ratio of $\frac{\kappa_{\text{b}}}{2}$ and ΔD_1 (58). It is maximized for a certain μ when the imaginary part of the denominator is zero ($\delta_{\text{b}} - \gamma_{\text{ab}}|A_0|^2 + \Delta D_1\mu = 0$), and decays when the mode

index deviates from μ. Therefore, if the FSR mismatch between the FH and SH is much greater than the SH total linewidth ($|\Delta D_1| \gg \frac{\kappa_b}{2}$), there is only one integer mode index μ that makes $J(\mu)$ significant. Although we are unable to directly characterize the linewidths of different SH mode resonances, this assumption should be valid in our condition. For lower-order SH modes, the external coupling rates are minimal (40), and therefore the total loss rates are dominated by the intrinsic loss rates. Suppose the intrinsic loss rate at SH is higher but in the order of that at FH (49), the SH loss rate is lower than the FSR difference $|\Delta D_1|$ (see Supplementary Note 1). While for higher-order SH mode $|\Delta D_1|$ reaches $\sim$ GHz for FH-SH3, so that $|\Delta D_1| \gg \frac{\kappa_b}{2}$ should still be valid. Thus the walk-off function $J(\mu)$ is only pronounced for one particular mode index μ, and can be considered zero for all the other integers. Note that the steady state SH field can also be written as $B_0 = g^* A_0^2 J(0)$. Without loss of generality we can omit the terms containing $J(-\mu)$, and considering the sideband generation at SH band is mainly via the sum-frequency process rather than the four-wave mixing involving far detuned SH, Eq. (5) can be simplified as:

$$B \approx B_0 + 2g^* A_0 a_1 J(\mu) e^{i\mu\phi} \tag{6}$$

Substitute Eq. (6) into Eq. (1) and separate the modal perturbations in the following form:

$$\begin{bmatrix} \frac{\partial a_1}{\partial t} \\ \frac{\partial a_2^*}{\partial t} \end{bmatrix} = \begin{bmatrix} -\frac{\kappa_a}{2} - i\delta_a - i\frac{D_{2,a}}{2}\mu^2 + 2i(\gamma_{aa} + J(\mu)|g|^2)|A_0|^2 & i\gamma_{aa}A_0^2 + igB_0 \\ -i\gamma_{aa}(A_0^*)^2 - ig^*B_0^* & -\frac{\kappa_a}{2} + i\delta_a + i\frac{D_{2,a}}{2}\mu^2 - 2i\gamma_{aa}|A_0|^2 \end{bmatrix} \begin{bmatrix} a_1 \\ a_2^* \end{bmatrix} \tag{7}$$

The eigenvalue of the matrix determines whether MI could initiate (54):

$$\Gamma(\mu) = -\frac{\kappa_a}{2} + iJ(\mu)|gA_0|^2 \pm \sqrt{|A_0|^4|\gamma_{aa} + |g|^2 J(0)|^2 - (\delta_a + \frac{D_{2,a}}{2}\mu^2 - 2\gamma_{aa}|A_0|^2 - J(\mu)|gA_0|^2)^2} \tag{8}$$

When the real part of the eigenvalue is greater than zero ($\text{Re}\{\Gamma(\mu) > 0\}$), the small perturbation at mode μ will be effectively amplified, and eventually leads to sideband and SF generation. The structure of computed MI is consistent with ref. (58) if only $\chi^{(2)}$ nonlinearity is considered with the approximation of single-sided coupling ($J(-\mu) \approx 0$). On the other hand, if FH-SH coupling strength g is set to 0, the derived MI also reduces to the form of conventional $\chi^{(3)}$ microresonators (54).

We use the following values for the MI simulation, i.e., $\kappa_a/2\pi = 90$ MHz, $\kappa_{ex,a}/2\pi = 60$ MHz, $\kappa_b/2\pi = 90$ MHz, $\Delta D_1/2\pi = -0.32$ GHz, $D_{2,a}/2\pi = -62.24$ kHz, $(\omega_b - 2\omega_a)/2\pi = 0.8$ GHz, $\gamma_{aa}/2\pi = 0.53$ Hz, $\gamma_{ab}/2\pi = 5.08$ Hz, $g/2\pi = 1$ kHz and $|s_{in}|^2 = 0.4$ W. Here, we consider the interacting SH to be the fundamental mode and assume the total linewidths of SH resonances are similar to that of FH resonances. We chose the cold-cavity resonance offset such that the SH resonance is initially blue-detuned, while being quickly compensated once the pump is coupled into the FH resonance. The self-phase and cross-phase nonlinear strengths are calculated based on the simulated mode overlaps (*26, 49*). For the FH-SH coupling rate, its magnitude is estimated from the photo-induced $\chi^{(2)}$ measured in Si_3N_4 microresonators (*40*). The numerically simulated MI gain is shown in Figure S2. Net gain is clearly observed whose peak position in mode index shifts proportionally with the pump detuning, explaining the successive switching of the primary comb FSR. While without the FH-SH coupling ($g = 0$), net gain is absent in the normal dispersion regime considering the simulation parameters above.
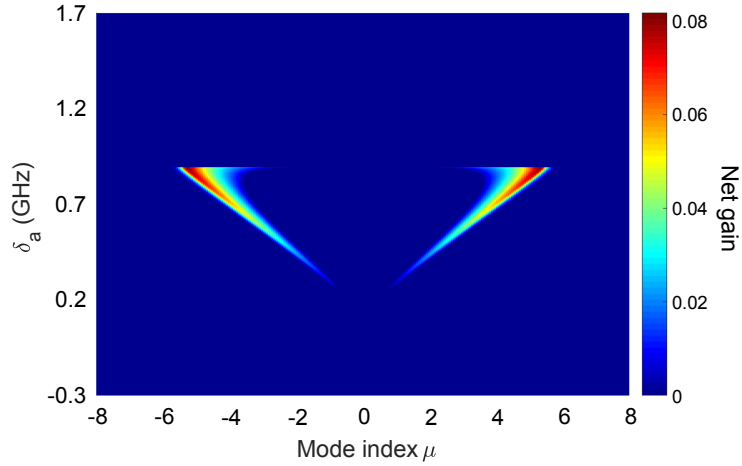

Figure S2: MI gain analysis for normal dispersion Si_3N_4 microresonators with FH-SH coupling. Using the derived MI equation and values present in this Supplementary Note, the net MI gain is simulated as a function of the pump detuning. It can be seen that the peak position of the net gain in mode index shifts proportionally with the pump detuning.

Supplementary Note 3. Experimental setup for comb generation

The experimental setup for optical poling as well as comb generation and characterization in a Si_3N_4 microresonator is shown in Figure S3. CW light from a C-band tunable laser is amplified and subsequently filtered with a tunable band-pass filter to remove the amplified spontaneous emission. Then, using a polarization controller and a lensed fiber, the light is coupled to the fundamental TE mode of the bus waveguide. The laser frequency is controlled via a function generator, which is slowly decreased so as to stably access the pump resonances of the microresonator. At the chip output, we collect both the FH and SH light using an optical lens, and separate them via a dichroic beam splitter. The FH light is collimated into an optical fiber and is then split into three parts. The first part is directed to a fast photodetector to measure the comb beatnote in an electrical spectrum analyzer. For the second part, a Waveshaper is programmed as a notch filter to reject the pump of the FH light, so that both the generated comb power and the pump transmission (the third part) can be measured in an oscilloscope. In terms of SH path, it is split into two parts, which are separately coupled back to optical fibers. One half is used to monitor the generated SH power in the oscilloscope, while the other half is directed to an optical spectrum analyzer (OSA). Since
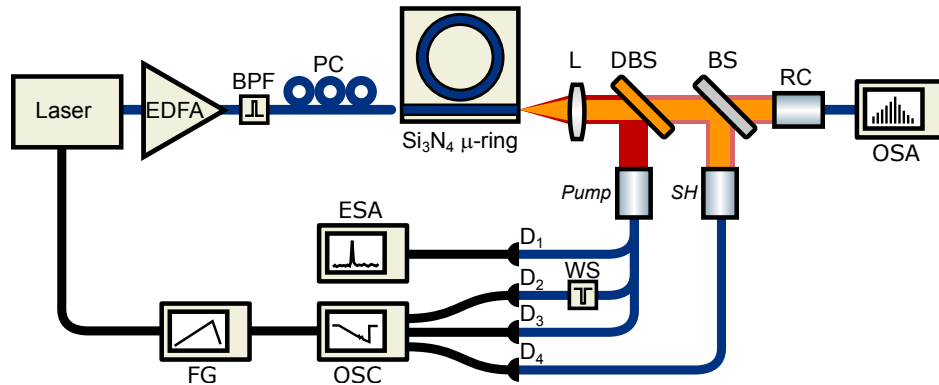

Figure S3: Experimental setup. EDFA: erbium-doped fiber amplifier; BPF: band-pass filter; PC: polarization controller; L: lens; DBS: dichroic beam splitter; BS: beam splitter; RC: reflective collimator; D_1: high speed FH detector; D_2, D_3: FH detector; D_4: SH detector; OSA: optical spectrum analyzer; FG: function generator; ESA: electrical spectrum analyzer; OSC: oscilloscope; WS: Waveshaper, programmed as a notch filter. Blue lines indicate optical fiber connection, while black lines indicate electrical wiring.

there is residual FH light in the SH path, the OSA is able to record both the optical spectra at FH and SH wavelengths.

Supplementary Note 4. Characterization of $\chi^{(2)}$ gratings at different pump detunings
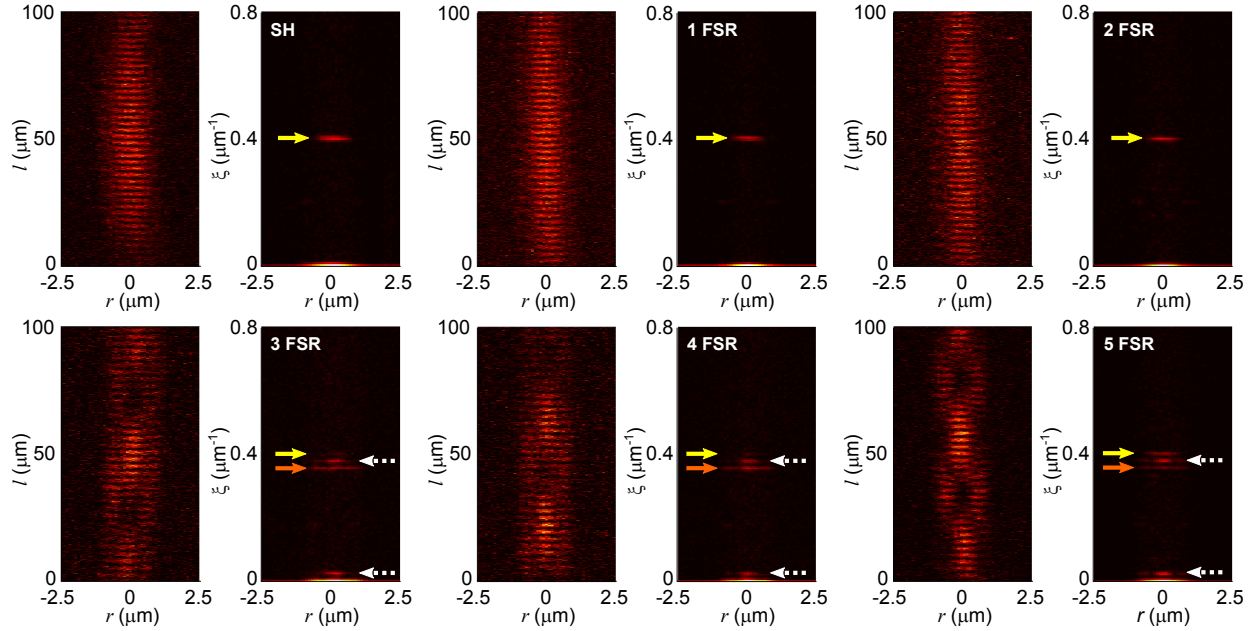

Figure S4: Grating images and their Fourier analyses at different pump detunings of the 1544.40 nm resonance. TPM images are measured when SH and SF coupled primary combs of different FSRs (1 FSR to 5 FSR) are generated. The Fourier transform of the images reveals the grating components. For SH, 1 FSR and 2 FSR cases, only FH-SH gratings are inscribed (yellow arrows). While for 3 FSR to 5 FSR cases, in addition to the FH-SH gratings, there are FH-SH-TH gratings (orange arrows) as well as components from the interference of the two gratings (dashed white arrows). Effective TH generation is observed in 3 FSR to 5 FSR cases.

In this note, we present the extended TPM characterization of the inscribed $\chi^{(2)}$ gratings for the 1544.40 nm pump resonance, as shown in Figure S4. Here, we measure the $\chi^{(2)}$ gratings at every characteristic detuning from only SH generation to primary combs of different FSRs. Note that the grating images in Figs. 2 a and d of the main text correspond to the SH and 5 FSR cases in Figure S4. At the beginning, only the FH-SH $\chi^{(2)}$ grating is inscribed in the microresonator enabling SH

generation. Since the FH-SH grating also phase-matches for the SF generation process, the SF coupled primary comb generation is supported by the same $\chi^{(2)}$ grating. This is confirmed experimentally by the TPM imaging of the inscribed gratings when the generated SF modes are 1 FSR and 2 FSR downshifted from the SH mode (see Figure S4 1 FSR and 2 FSR cases). For both cases, $\chi^{(2)}$ gratings with the same spatial frequencies (yellow arrows) as the SH case are measured in the microresonator, and no other grating components are observed. Further pump detuning leads to the further FSR switching of the SF coupled primary combs as well as the effective TH generation. As shown in the 3 FSR to 5 FSR cases of Figure S4, we observe superimposed grating structures and analyze them with Fourier transform. In addition to the spatial frequency of the initial FH-SH grating, a secondary spatial frequency (orange arrow) and their interference components (dashed white arrows) are identified. Here the secondary gratings have the same spatial frequencies for 3 FSR to 5 FSR cases. They are the FH-SH-TH gratings, which phase-match the cascaded harmonic generation process and are again inscribed via the photogalvanic effect.

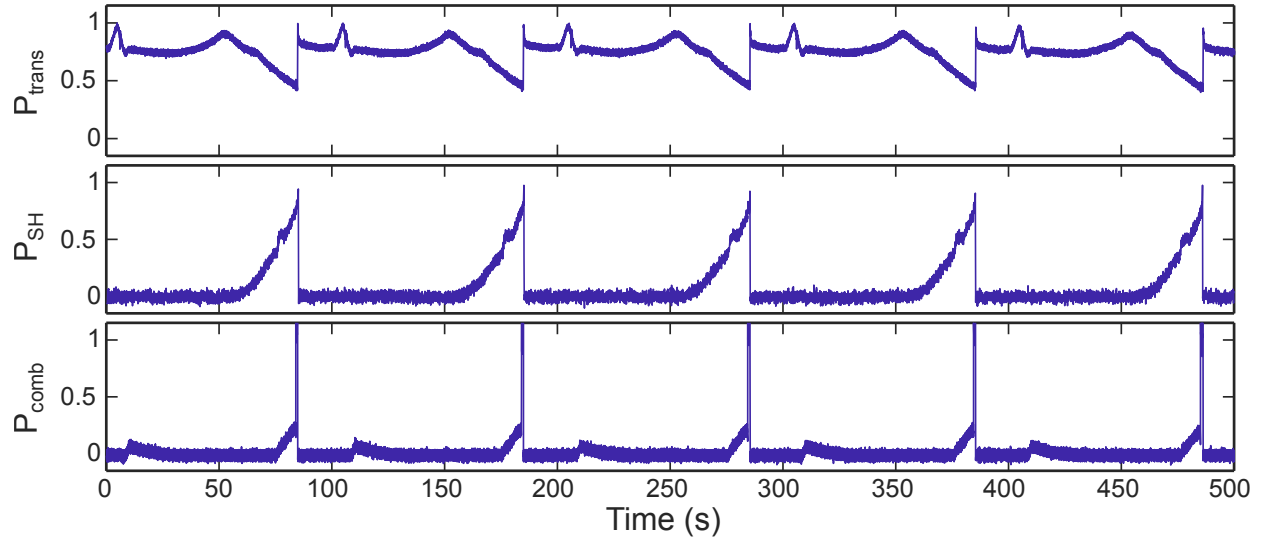**Supplementary Note 5. Deterministic broadband comb generation**

Figure S5: Deterministic broadband comb generation. Pump transmission (P_{trans}), generated SH power (P_{SH}) and comb power (P_{comb}) recorded during five consecutive laser frequency scans across the 1552.34 nm pump resonance. The sharp increase of the measured comb power indicates the generation of the broadband comb state.

Here, we show that the generated broadband dark pulse microcomb (see Fig. 4 in the main text) can be accessed in a deterministic fashion. Figure S5 illustrates the transmission curves of the pump, SH, and comb power when sweeping across the $1552.34\,\mathrm{nm}$ resonance for five consecutive times. In each consecutive sweep, the primary comb at FH is initiated after the SH generation, and is finally evolved into the broadband comb state in a deterministic manner without transitioning through a chaotic region.